EES Catalysis

MINIREVIEW

View Article Online
View Journal | View Issue

Cite this: *EES Catal.*, 2024, 2, 545

Unconventional intermetallic noble metal nanocrystals for energy-conversion electrocatalysis

Zhuhuang Qin, Tanyuan Wang, Zhangyi Yao and Qing Li *

Structurally ordered intermetallic noble metal nanocrystals (NCs) with unconventional phases exhibit impressive catalytic activity and stability resulting from the novel atomic stacking patterns and coordination environments, and thus have attracted extensive attention for energy-conversion electrocatalysis in recent years. In this mini-review, recent advances in developing unconventional intermetallic noble metal NCs for high-performance electrochemical energy conversion technologies are highlighted. First, the theoretical aspects of the relationship between the crystal phases of metal alloys and their electrocatalytic performance are introduced, and the obstacles in the preparation of unconventional intermetallic noble metal NCs are described. Then, several representative examples are presented to highlight the applications of unconventional noble metal-based intermetallic NCs as electrocatalysts for different electrocatalytic reactions. Finally, perspectives and future opportunities for the rational design and preparation of unconventional intermetallic NCs for sustainable electrochemical devices are discussed.

Received 7th October 2023,
Accepted 28th November 2023

DOI: 10.1039/d3ey00248a

rsc.li/eescatalysis

Broader context

Due to the advantages of high conversion efficiency and zero carbon emission, sustainable electrochemical energy conversion technologies (*e.g.*, proton exchange membrane fuel cells and electrochemical water splitting) have been extensively regarded as the solution for the energy and environmental crisis. However, the efficiency of electrochemical energy conversion technologies is limited by some key electrochemical processes (*e.g.*, the HER, HOR, OER and ORR), which demand an enormous amount of precious metal catalysts to overcome the excessive reaction overpotentials. Therefore, it is crucial to rationally design noble metal electrocatalysts with outstanding performance for the corresponding electrocatalytic reactions. With impressive activity and durability for diverse catalytic reactions, noble metal-based intermetallic nanocrystals have been the topic under intensive investigation recently. However, current efforts mainly focus on the intermetallic systems with cubic close-packed structures such as $L1_0$ and $L1_2$ structures. The search for new types of crystal structures with unconventional atomic arrangements and coordination environments cannot be delayed. This mini-review summarizes the applications of various unconventional intermetallic noble metal-based nanocrystals in energy-conversion electrocatalysis and provides a feasible direction for developing novel metal electrocatalysts with much enhanced performance.

1. Introduction

Electrochemical energy-conversion technology is a promising strategy for the development of clean and sustainable energy sources.[1–4] In particular, hydrogen energy conversion technologies such as proton exchange membrane fuel cells (PEMFCs), which directly convert the chemical energy stored in hydrogen into electrical energy, have the advantages of high conversion efficiency, high energy density and zero carbon emission.[5–8] In addition, electrochemical water splitting can sustainably convert renewable electrical power into hydrogen with a high calorific combustion value, which features the high-purity hydrogen and environmental friendliness compared to the production of hydrogen from steam reforming.[9–11] The combination of PEMFCs and electrochemical water splitting would offer a solution for solving the energy shortage and environmental pollution problems. However, their large-scale commercialization is primarily hampered by the sluggish kinetics of some key electrocatalytic reactions, *e.g.*, the oxygen reduction reaction (ORR),[12–14] oxygen evolution reaction (OER),[15,16] hydrogen evolution reaction (HER),[17] and hydrogen oxidation reaction (HOR).[18] These reactions usually require a substantial amount of precious metal catalysts (Pt, Ir, Ru, Pd, *etc.*) to overcome the excessive reaction overpotentials. Therefore, reducing the usage of precious metals and improving their catalytic performance have become the research focus in the past few decades.

Many investigations have demonstrated that alloying noble metals with transition metals is an effective strategy for improving the performance of noble metal-based catalysts.[19–23] The introduction of transition metals can result in the shift of the d-band

State Key Laboratory of Material Processing and Die & Mould Technology, School of Materials Science and Engineering, Huazhong University of Science and Technology, Wuhan, Hubei 430074, China. E-mail: qing_li@hust.edu.cn

center through the ligand effect and the strain effect, which significantly affect the adsorption energies of the intermediates, so as to enhance the kinetics of catalytic reactions.[24] For example, Pt–M (M = Fe, Co, Ni, *etc.*) alloy catalysts exhibit superior ORR activity over Pt/C, which is attributed to their weaker binding with oxygenated intermediates.[25] However, owing to the susceptibility of transition metals to dissolution (*e.g.*, in acidic electrolytes and under oxidative conditions), the durability of alloy catalysts in harsh electrochemical environments is poor.[26] Interestingly, it has been demonstrated that the phase transformation from disordered alloys to structurally ordered intermetallic NCs could achieve the enhanced stability of alloy electrocatalysts, which is attributed to the strong 3d–5d orbital interactions and more negative enthalpy of formation of intermetallic NCs.[4] Taking structurally ordered $L1_0$-PtM catalysts as examples, the electrochemical measurements show significantly less leaching of their non-precious metal components (M) than disordered alloy phases (face-centered cubic, fcc) during electrochemical cycling.[27]

Although some advancements have been made in the phase engineering of metal electrocatalysts, current research studies mainly focus on intermetallic bi- or tri-metallic systems with cubic close-packed structures such as $L1_0$ and $L1_2$ structures.[21,28] It is of vital significance to explore and rationally design new types of crystal structures with different atomic arrangements and coordination environments (*e.g.*, bond lengths and coordination numbers), which could potentially contribute to the activity and durability of the metal electrocatalysts. Here, we define crystal structures that differ from the cubic close-packed type (*e.g.*, $L1_0$ and $L1_2$) as unconventional intermetallic NCs. Some typical examples of unconventional intermetallic phases include body centered cubic phases (*e.g.*, B2 and DO_3), hexagonal close-packed phases (*e.g.*, $B8_1$ and $L1_1$) and topologically close-packed phases (*e.g.*, A15 and C15) (Fig. 1). Specifically, the body centered cubic phase is characterized by a coordination number of 8, which is lower compared to the cubic close-packed phase. As an example, for B2-PdCu, the Pd atom lies at the (0, 0, 0) site and the Cu atom at the (1/2, 1/2, 1/2) site in the unit cell, and the isolated Pd atom is present in the center of the cube composed of eight Cu atoms. In addition, similar to the cubic close-packed phase, the hexagonal close-packed phase also features close-packing, with the exception that the close-packed surfaces of the hexagonal close-packed phase are only composed of monometallic atoms. Taking $B8_1$-PtPb as an example, the atoms are located at (0, 0, *z*), (1/3, 2/3, *z*), and (2/3, 1/3, *z*) sites in the unit cell. The crystal structure of $B8_1$-PtPb can be divided into Pt and Pb layers along the *c* axis, and Pt layers are separated by Pb atomic layers. In particular, for the Pt–M topologically close-packed phase, alloying with Pt/M ratios of 1/3 and 2/1 favors A15- (space group: $Pm\bar{3}n$) and C15-ordered structures (space group: $Fd\bar{3}m$), respectively, which possess more complex crystal structures with higher coordination numbers and packing densities than geometrically close-packed phases. For example, the coordination numbers are 12 (6 Pt + 6 M) for the Pt atom and 16 (12 Pt + 4 M) for the M atom in C15-Pt_2M, while the coordination numbers are 12 (4 Pt + 8 M) for the Pt atom and 12 (8 Pt + 4 M) for the M atom in $L1_0$-PtM. These specific coordination environments would potentially affect the binding energies of the adsorbates on the catalyst surface and alter the reaction kinetics of the catalytic process.[29] Additionally, it is generally recognized that the increase in the Pt–M/M–M bond ratio serves to alleviate the corrosion of the reactive M atom in the electrochemical environment and thus contributes to the stability of the Pt–M alloy system.[30] In comparison to $L1_2$-Pt_3M and $L1_0$-PtM, C15-Pt_2M possesses a higher Pt–M/M–M bond ratio (*i.e.*, 2/3, 2/1, and 3/1 for $L1_2$-Pt_3M, $L1_0$-PtM, and C15-Pt_2M, respectively), which is anticipated to achieve outstanding stability.

This mini-review summarizes the design and preparation of various unconventional intermetallic noble metal-based NCs and their applications in energy-conversion electrocatalysis. Firstly, we provide fundamental insights into the significance

Zhuhuang Qin

Zhuhuang Qin received his bachelor's degree in materials science and engineering from Hunan University in 2021. He is now pursuing his master's degree in the Huazhong University of Science and Technology under the supervision of Prof. Qing Li. His research interests include energy materials and electrocatalysis.

Qing Li

Qing Li is a professor at the School of Materials Science and Engineering in the Huazhong University of Science and Technology (HUST), China. He received his PhD in Chemistry from Peking University in 2010 and then worked as a post-doctoral research associate at the Los Alamos National Laboratory (2011–2013) and Brown University (2013–2015). He has co-authored more than 160 papers with >15 000 citations. His current research interests focus on developing advanced electrocatalysts and devices for fuel cells and water electrolysis.

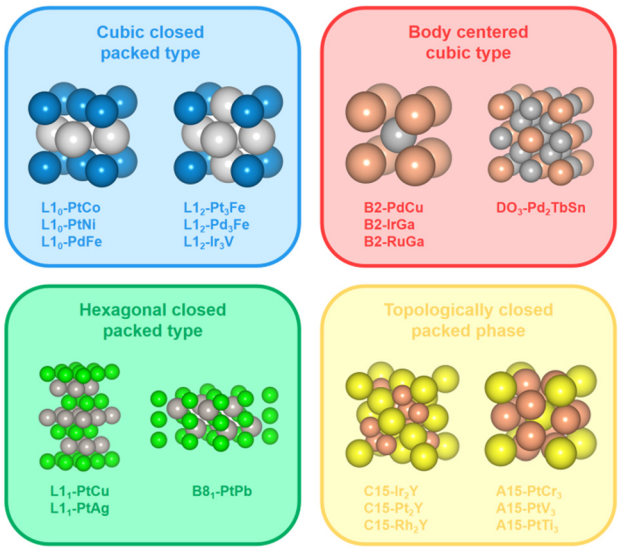

Fig. 1 Illustration of various crystal structures of intermetallic nanocatalysts.

of unconventional intermetallic structures for electrocatalysis and present an in-depth analysis of how to synthesize these unique metal electrocatalysts from both thermodynamic and kinetic perspectives. Then we summarize the recent research progress of unconventional intermetallic noble metal-based compounds in different electrocatalytic reactions, such as the HER, ORR and EOR. Finally, we outline the challenges and prospects for developing unconventional intermetallic NCs for sustainable electrochemical energy conversion technologies.

2. Fundamentals of unconventional intermetallic NCs

2.1. Theoretical aspects of electrocatalysis

A thorough understanding of the adsorption behavior of substances on the catalyst surface is essential for the rational design of catalysts. Theoretical studies demonstrate that the binding strength between the catalyst surface and the intermediates has a crucial influence on the reaction rate and catalytic activity.[30] According to Sabatier theory, the rate of the catalytic reaction would be maximum when the adsorption strength of species reaches an appropriate value.[31] In unconventional intermetallic NCs, compared to $L1_0$/$L1_2$ structures, the distinctive bond lengths and coordination numbers in their crystal structures can alter the adsorption strength between the catalyst surface and the adsorbed species, leading to a remarkable contribution to the electrocatalytic performance of the electrocatalyst.[32] Taking intermetallic $PtBi_2$ nanoplates for the formic acid oxidation reaction (FAOR) as an example, cubic β-$PtBi_2$ features a relatively long Pt–Pt distance compared to trigonal γ-$PtBi_2$.[33] The excellent catalytic performance and CO poisoning tolerance have been observed in cubic β-$PtBi_2$, wherein the isolated Pt atoms diminish the adsorption of CO. Another example is the cubic $Pd_{17}Se_{15}$ NC for the alkaline ORR.[29] The Pd atom in cubic $Pd_{17}Se_{15}$ is coordinated with more Se atoms, resulting in a higher valence state with respect to the orthorhombic Pd_7Se_4, which contributes to more charge transfer from the cubic $Pd_{17}Se_{15}$ surface to the oxygenated species. Therefore, cubic $Pd_{17}Se_{15}$ achieves a higher mass activity and specific activity than orthorhombic Pd_7Se_4. Apart from modulating the adsorption strength of catalysts on intermediates, regulating the spatial orientation of the adsorbed species and constructing a favorable adsorption configuration on the catalyst surface are also regarded as powerful approaches to facilitate the kinetics of electrocatalytic reactions.[34–36] For example, the high-density Cu–Pd pairs in B2-PdCu could adjust the adsorption configuration of the *CO intermediate to enrich *CO coverage and promote CO-to-acetate conversion during CO_2 electroreduction.[37] Surface-enhanced infrared absorption spectroscopy and DFT calculations demonstrate that surface *CO species on B2-PdCu are mainly adsorbed on $CuPd_2$ hollow sites in a triple-bond mode, while being absent on Cu electrodes. As a result, the high coverage of *CO on B2-PdCu promotes C–C coupling and inhibits H_2 evolution.

The stability of a complicated electrochemical environment is also a worthwhile consideration with respect to the design of electrocatalysts. The formation energy of crystal structures can be considered as a descriptor of the stability of NCs in electrocatalytic processes. For example, in the case of $L1_0$-PtM (M = Fe, Co, Ni, Zn) alloy systems, a negative correlation between the formation energy of $L1_0$-PtM and the vacancy formation energy of the M atom is established.[38,39] $L1_0$-PtZn exhibits a higher structural stability among the $L1_0$-PtM systems, which is closely related to the fact that $L1_0$-PtZn has a lower formation energy among others. Compared to $L1_0$-structures, some unconventional crystal structures have more negative structure formation energies (*e.g.*, −0.566 eV per atom, −1.022 eV per atom, and −1.084 eV per atom for $L1_0$-PtZn, $D0_{24}$-Pt_3Zr, and C15-Pt_2Y, respectively).[40] Therefore, the design of unconventional intermetallic NCs with more negative structure formation energies is a valid concept for the fabrication of highly stable catalysts based on thermodynamic principles. In addition, the atomic dissolution of NCs is among the primary factors responsible for the degradation of catalyst performance. As undercoordinated atoms are preferentially solubilised in electrochemical processes, an increased proportion of high coordination atoms on the surface would contribute to the stability of the catalysts.[41] For example, *in situ* inductively coupled plasma (ICP)-mass spectroscopy (MS) measurements reveal that the amount of Pt atoms dissolved decreases in the opposite order as the coordination number of surface atoms: Pt(110) < Pt(100) < Pt(111).[42] From this point of view, the topologically close-packed phases possessing a high coordination number, *e.g.* A15, C15, *etc.*, are expected to be electrocatalysts with enhanced durability.

2.2. Challenges in synthesizing unconventional intermetallic NCs

The aforementioned theoretical studies demonstrate that the preparation of unconventional intermetallic NCs is an effective way to enhance both the activity and stability of electrocatalysts. In this section, the thermodynamic and kinetic obstacles

associated with the preparation of unconventional intermetallic noble metal compounds will be elucidated.

Thermodynamic perspectives. According to the phase diagram of noble metal alloys, the unconventional intermetallic compounds are usually placed in the middle and low-temperature regions with narrow distributions, which indicates that the exact atomic composition of the nanoparticles is essential for the synthesis of unconventional intermetallic NCs. For example, the PtCr nanoparticles can be transformed into unconventional A15-$PtCr_3$ intermetallic NCs at a moderate temperature when the metal content in the PtCr nanoparticle is close to a Pt : Cr ratio of 1 : 3 (Fig. 2a). As co-reduction is a direct and universal method for the efficient synthesis of NCs, the key to the successful synthesis of unconventional intermetallic NCs is the selection of a suitable reducing agent to rationally modulate the content of metals in the nanoparticles. It should be pointed out that the tendency of the metal-containing precursor to be reduced is related to the standard reduction potential of the metal component.[43–45] Specifically, the metal-containing precursors with high standard reduction potentials are much more easily reduced than the ones with low reduction potentials for the identical situation. Arguably, owing to the relatively high standard reduction potentials of late transition metals (Fig. 2b), it is more easy to fabricate N–L (N for noble metals and L for late transition metals) intermetallic blocks, whose thermodynamically stable crystal structures belong to the cubic close-packed phase. For instance, the $L1_0$ or $L1_2$-PtM or PdM (M = Fe, Co, Ni, *etc.*) structures have been abundantly discussed.[4,21,28] In comparison, unconventional intermetallic compounds are mainly found in the phase diagrams of noble metal alloys with p-block metals, early transition metals or rare earth metals. However, these metals (especially the early transition and rare earth metals) with much lower standard redox reduction potentials than the stability range of water can hardly be reduced by the usual reducing agents and tend to form metal oxides in aqueous or organic solvents.[40] Precisely controlling the content of p-block, early transition or rare earth metals in nanoparticles through a wet-chemical method has become a challenging and impractical route. To this end, the reduction of these metal ions to form unconventional noble metal-based intermetallic NCs would be only achieved by using strong reducing agents in the absence of water and oxygen. For example, B19-IrMo and Pt_5Ce with the hexagonal phase can be successfully prepared by the high-purity hydrogen reduction procedure at high temperatures.[46,47]

Kinetic perspectives. The driving force for a specific phase transition is often related to the difference in the crystal structures of the parent phase and produced phase.[32] Obviously, the degree of lattice mismatch between the parent phase and the produced phase is the dominant determinant of interfacial free energy, which increases as the matching of the atoms on both sides of the interface decreases. It is noted that the lattice mismatch arises from the differences in lattice parameters. Thus, the calculation of the change in lattice

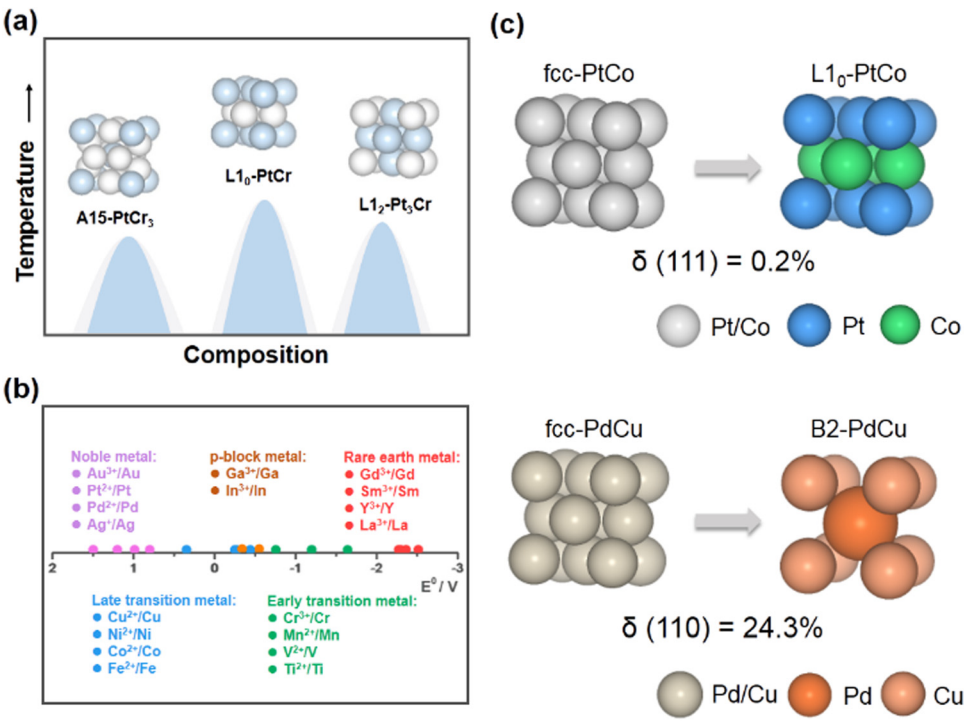

Fig. 2 (a) Schematic representation of the change in the crystal structure of PtCr NCs with increasing Pt content at normal temperature based on the phase diagram. (b) Standard reduction potentials of different metal ions. (c) Schematic illustration of the phase transition from fcc-PtCo to $L1_0$-PtCo and fcc-PdCu to B2-PdCu, and the corresponding degree of lattice mismatch.

parameters in the produced phase with respect to the parent phase is an effective method to quantify the degree of lattice mismatch (δ):

$$\delta(hkl) = \frac{d_\beta(hkl) - d_\alpha(hkl)}{d_\alpha(hkl)} \times 100\% \quad (1)$$

where $d_\beta(hkl)$ and $d_\alpha(hkl)$ represent the interplanar spacing of the (hkl) face in the newly formed and parent phases, respectively. Taking the transformation of fcc-PtCo into $L1_0$-PtCo as an example, the degree of lattice mismatch between the (111) face of fcc-PtCo and $L1_0$-PtCo is only 0.2% (Fig. 2c). In this context, a lower interfacial energy and larger driving force exist between two similar crystal phases, which usually favour the phase transition process. In contrast, there is a large degree of lattice mismatch of 24.3% in the transformation of fcc-PdCu into unconventional B2-PdCu, which means a higher energy barrier to achieve atomic rearrangement. Therefore, an appropriate increase in the heat treatment temperature would effectively speed up the atom-diffusion process to prepare unconventional noble metal-based intermetallic NCs. Please note that the process of phase transition fails to occur at temperature that is too high, due to the negative entropy change ($\Delta S^{nano}_{d\to o} < 0$) during the ordering process.[4]

Thermodynamic and kinetic analyses allow us to develop a fundamental understanding of the preparation of unconventional intermetallic noble metal compounds. Consequently, to rationally design a synthesis scheme for unconventional intermetallic noble metal-based NCs, we need to identify specific underlying physicochemical processes and their corresponding diffusion modes.

3. Applications of unconventional intermetallic noble metal NCs

Unconventional intermetallic noble metal NCs with unique atomic arrangements show excellent performance for different catalytic reactions, such as the HER, ORR and EOR. In this

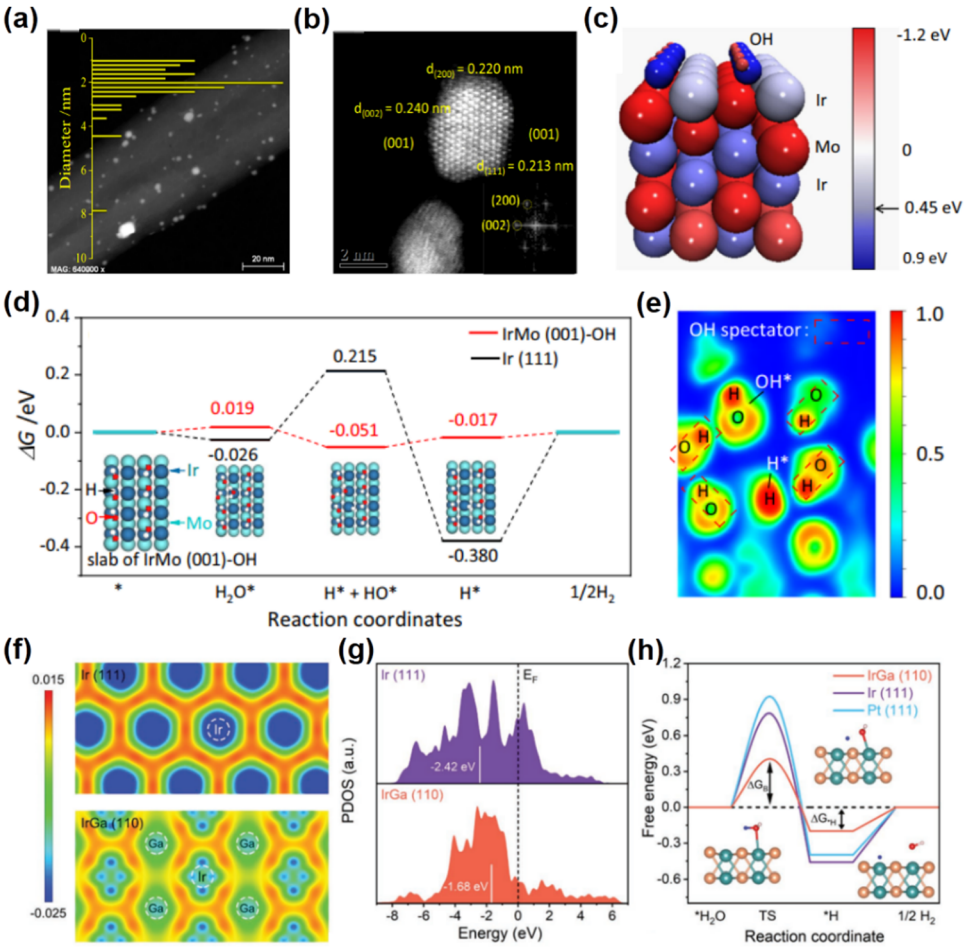

Fig. 3 (a) The high-angle annular dark-field scanning transmission electron microscopy (HAADF-STEM) image of B19-IrMo nanoparticles. (b) Aberration-corrected HADDF-STEM image of B19-IrMo nanoparticles. (c) Image of Bader charge for B19-IrMo. (d) Gibbs free energy diagram of the HER of the IrMo (001)-OH slab. (e) Electron localization function plot of the B19-IrMo nanoparticles. (a)–(e) Reproduced with permission from ref. 46. Copyright 2022, Nature Publishing Group. (f) The charge density difference images of IrGa(110) and Ir(111). (g) The partial density of states of Ir sites in IrGa(110) and Ir(111). (h) Gibbs free energy diagram of the HER on IrGa(110), Pt(111), and Ir(111). (f)–(h) Reproduced with permission from Ref. 48. Copyright 2022, John Wiley and Sons.

section, some representative intermetallic noble metal-based NCs with unconventional phases and their structure-performance correlations are presented.

Hydrogen evolution reaction

The hydrogen evolution reaction (HER) represents an essential process in water splitting, which conveniently provides high-quality hydrogen. Recently, unconventional noble metal-based intermetallic NCs with novel crystal structures have attracted great attention due to their exceptional properties for the HER. In particular, many unconventional noble metal-based intermetallic NCs are prepared by the two-step method of impregnation and annealing reduction, due to the features of straightforward operation. For example, B19-IrMo intermetallic NCs supported on carbon nanotubes (IrMo/CNT) were synthesized by reductive annealing at 800 °C under a H_2/Ar atmosphere (Fig. 3a and b).[46] The lattice parameters of B19-IrMo are determined to be a = 2.775 Å, b = 4.463 Å, c = 4.862 Å and $\alpha = \beta = \gamma = 90^\circ$. B19-IrMo/CNT exhibits a better HER activity under both acidic and alkaline conditions compared to the commercial Pt/C catalyst, *i.e.*, the overpotentials of 17 mV (1.0 M KOH) and 13 mV (0.5 M H_2SO_4) at a current density of 10 mA cm^{-2}. Additionally, B19-IrMo/CNT possesses superior stability in both alkaline and acidic electrolytes, showing a negligible decrease of catalytic activity after 10 000 potential cycles. DFT calculations show that the OH species adsorbed on the B19-IrMo intermetallic compound could bind to the OH generated by water dissociation through hydrogen bonding, facilitating a thermodynamically favorable water dissociation process under alkaline conditions (Fig. 3c–e). Another example of an attractive unconventional noble metal-based intermetallic compound is B2-IrGa. Owing to the relatively high standard reduction potential of Ga (*e.g.*, E_0 (Ga/Ga^{3+}) = −0.549 V *vs.* the standard hydrogen electrode), it is more easy to precisely control a specific composition (*i.e.*, Ir : Ga ratio of 1 : 1) in nanoparticles to prepare unconventional intermetallic B2-IrGa NCs. For example, the B2-IrGa intermetallic compounds anchored on the nitrogen-doped reduced graphene oxides (IrGa/N-rGO) were prepared by a two-step method of impregnation and heat treatment at 800 °C.[48] B2-IrGa has a space group of $Pm\bar{3}m$. Especially, the unit cell parameters of B2-IrGa are $a = b = c$ = 3.06 Å and $\alpha = \beta = \gamma = 90^\circ$. In this crystal structure, the Ir atoms occupy the center of the unit cell, while the Ga atoms are located at the eight vertices of the unit cell. The isolated Ir atom in B2-IrGa is surrounded by eight Ga atoms with lower electronegativity, which provides electron-rich environments for the Ir atom and results in a donor–acceptor architecture. The electron transfer between the Ir sites and the adsorbed species is promoted by the electron-rich Ir sites in the body-centered cubic structure, effectively reducing the energy barriers for the HER (Fig. 3f–h). Experimentally, IrGa/N-rGO exhibits an overall superior water splitting performance in an alkaline electrolyte, *i.e.*, the low overpotentials of 22 mV at 10 mA cm^{-2} for the HER and 258 mV at 10 mA cm^{-2} for the OER. Remarkably, when IrGa/N-rGO is applied as the cathode and the anode catalyst respectively for alkaline overall water splitting, the IrGa/N-rGO||IrGa/N-rGO system requires a low voltage of 1.51 V in the cell to achieve 10 mA cm^{-2} and shows a negligible degradation within 100 h, significantly outperforming Pt/C||IrO_2/C systems. Additionally, the HER performances of B2-PdCu and B2-RuGa have been investigated, both of which exhibit lower overpotentials compared to commercial Pt/C.[49,50]

In addition to the two-step method of impregnation and annealing reduction, the molten salt-assisted synthesis method, which facilitates efficient diffusion and reaction of the reactants, has been adopted as an environmentally friendly approach toward a range of intermetallic silicides (PtSi, RhSi, Ru_2Si_3, IrSi), germanide ($RuGe_3$) and stannides (Ru_3Sn_7, $IrSn_2$, $PdSn_3$, $PdSn_2$).[51] Especially, the PtSi intermetallic nanocrystal (space group: *Pnma*) with the orthorhombic phase exhibits outstanding electrocatalytic performance for the HER with low overpotentials of 22, 39 and 66 mV at 10 mA cm^{-2} in acidic, alkaline and neutral electrolytes, respectively. The lattice parameters of orthorhombic PtSi intermetallic NCs are determined to be a = 5.577 Å, b = 3.587 Å, c = 5.916 Å and $\alpha = \beta = \gamma = 90^\circ$. Theoretical calculations show that the alloying of Pt and Si weakens the binding energy between Pt and H atoms, and the orthorhombic PtSi intermetallic compounds possess preferable binding energies to H atoms compared to other noble-metal-based carbon-group intermetallic compounds and Pt/C, further promoting the production of hydrogen during the HER process. Also, this result provides a feasible idea for developing other kinds of metal-based carbon-group intermetallic phases with excellent activity in the HER and beyond.

Oxygen reduction reaction

The oxygen reduction reaction that takes place at the cathode of the fuel cell determines the overall efficiency of the fuel cell. Currently, unconventional Pt-based intermetallic compounds are receiving much attention due to their excellent electrocatalytic activity and enhanced stability for the ORR. For instance, the $B8_1$-PtPb/fcc-Pt core–shell nanosheets were prepared using one-pot synthesis.[52] These $B8_1$-PtPb/fcc-Pt core–shell nanosheets were synthesized directly by heating a mixture of octadecene and oleylamine at 160 °C for 5 h. Especially, the unit cell parameters of $B8_1$-PtPb are $a = b$ = 4.388 Å, c = 5.579 Å, $\alpha = \beta = 90^\circ$ and $\gamma = 120^\circ$. Structural characterization reveals that the lattice mismatch between the fcc-Pt shell and $B8_1$-PtPb core results in biaxial strain over the Pt shell. DFT calculations show that the appropriate tensile strain on the Pt(110) facets can weaken the bond energy between the Pt atom and O atom, thus enhancing the ORR activity. Compared to Pt/C and PtPb nanoparticles, the $B8_1$-PtPb/Pt nanosheets show the optimum performances for the ORR. The specific activity (SA) and mass activity (MA) are 7.8 mA cm^{-2} and 4.3 A mg_{Pt}^{-1} at 0.9 V *versus* the reversible hydrogen electrode (RHE), respectively. The strong interaction between Pt and Pb in the intermetallic compound also resulted in excellent stability. After 50 000 cycles, there is only a slight decay in MA and SA. Recently, examples of Pt–lanthanide alloys have presented opportunities for customizing electronic properties and synergistic surface reactivity.[53] Furthermore, the atomically ordered

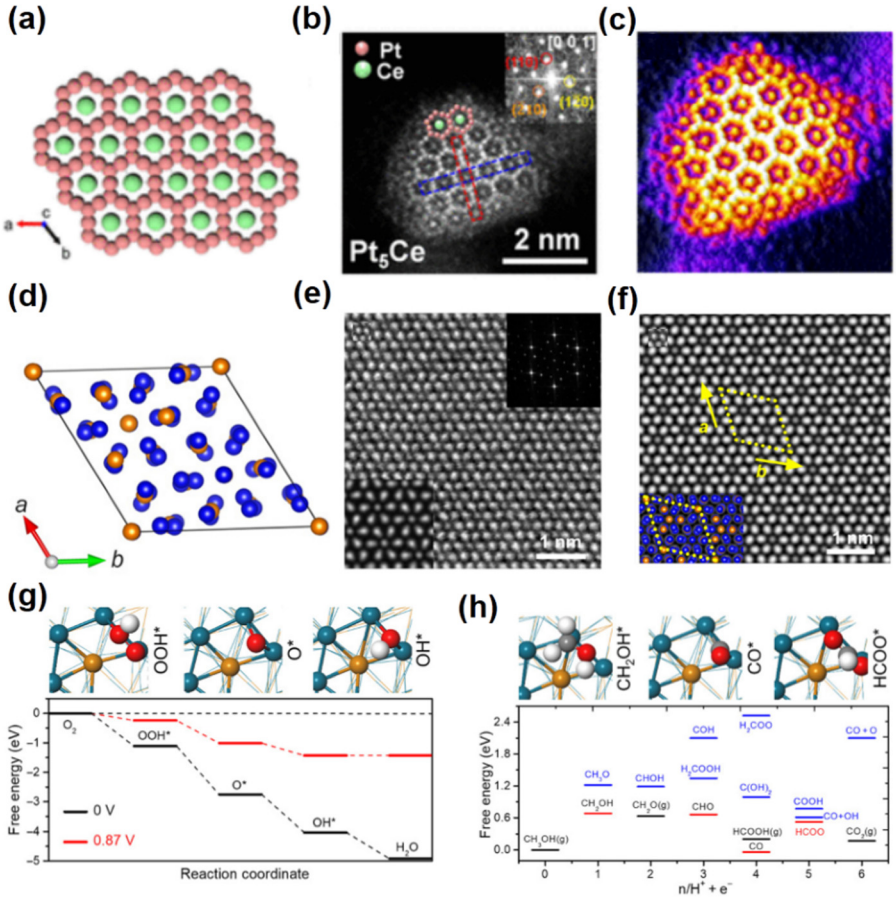

Fig. 4 (a) Crystal structure of Pt_5Ce. (b) Aberration-corrected HADDF-STEM image of a Pt_5Ce particle. (c) 3D atom-overlapping Gaussian-function image. (a)–(c) Reproduced with permission from Ref. 54. Copyright 2022, American Chemical Society. (d) Crystal structure of $Pd_{20}Te_7$. (e) Aberration-corrected HAADF-STEM images of $Pd_{20}Te_7$ nanosheets. (f) Structure model of $Pd_{20}Te_7$ nanosheets. (g) Calculated free energy profiles at 0 and 0.87 V for the ORR on $Pd_{20}Te_7$, respectively. (h) Free energies of the possible intermediates on $Pd_{20}Te_7$ nanosheets during the MOR. (d)–(h) Reproduced with permission from Ref. 56. Copyright 2020, American Association for the Advancement of Science.

Pt–lanthanide intermetallic compounds are expected to show significantly improved performance and stability for the ORR. For example, Pt_5Ce with the hexagonal phase was synthesized by the interparticle-distance-dependent hydrogen spillover approach (Fig. 4a–c).[54] In particular, the reduction of Ce around Pt is facilitated by decreasing the inter-particle distance to enlarge the available area for hydrogen spillover, which guarantees the alloying of Pt with a sufficient fraction of Ce to promote the formation of the thermodynamically favourable intermetallic Pt_5Ce NCs with the hexagonal phase. The unit cell parameters of Pt_5Ce are $a = b = 5.385$ Å, $c = 4.456$ Å, $\alpha = \beta = 90^\circ$ and $\gamma = 120^\circ$. A Pt-rich shell exists on the surface of hexagonal Pt_5Ce nanoparticles, which is revealed by energy-dispersive X-ray spectroscopy line scanning and aberration-corrected HAADF-STEM. Benefiting from the compressive strain induced by the Pt_5Ce/Pt layer core/shell structure, the binding energy of the oxygen-containing species on Pt sites would decrease. Thus, the improved ORR performance compared to Pt/C under acidic conditions is found, with specific activity (SA) and mass activity (MA) of 1.05 mA cm^{-2} and 0.69 A mg_{Pt}^{-1} at 0.9 V *versus* RHE, respectively.

Similar to unconventional Pt-based intermetallic compounds, the performance of Pd-based nanocatalysts can also be improved by appropriate atomic ordering engineering. For example, controlling the crystal structure of Pd–Bi NCs provides an attractive route to improve their electrocatalytic activity and stability for the ORR in alkaline media. By changing only the type of Pd precursor under the same conditions, the monoclinic Pd_5Bi_2 and conventional fcc-Pd_3Bi NCs with similar sizes and morphologies could be precisely synthesized by a simple one-step synthesis method.[55] Interestingly, the monoclinic Pd_5Bi_2 exhibits a better alkaline ORR performance than conventional fcc-Pd_3Bi due to the difference in the atomic arrangement. The unit cell parameters of monoclinic Pd_5Bi_2 are $a = b = 7.786$ Å, $c = 6.878$ Å, $\alpha = \beta = 65.05^\circ$ and $\gamma = 44.64^\circ$. Pd_5Bi_2/C shows a MA of 2.05 A mg_{Pd}^{-1} at 0.9 V *versus* the RHE for the ORR in alkaline media. After 10 000 cycles, the MA of Pd_5Bi_2/C is still 1.52 A mg_{Pd}^{-1}, which is 3.6 times, 16.9 times and 21.7 times higher than those of fcc-Pd_3Bi/C, commercial Pd/C and Pt/C, respectively. In practical ethanol fuel cell operation, CO-like species produced by permeation and oxidation of methanol from the anode to the cathode can adsorb strongly on the

surface of the precious metal surface, affecting the overall efficiency of the fuel cell. Therefore, it is ideal to design cathode catalysts with both high ORR activity and excellent methanol tolerance. Recently, intermetallic $Pd_{20}Te_7$ nanosheets with outstanding ORR performance and methanol tolerance have been reported (Fig. 4d–f).[56] The lattice parameters of $Pd_{20}Te_7$ are determined to be $a = b = 11.9$ Å, $c = 11.6$ Å, $\alpha = \beta = 90^\circ$ and $\gamma = 120^\circ$. Based on the crystal structure analysis, the location of the Pd atom deviates from the ideal lattice of a hexagonal close-packed arrangement, which creates a bridge site for the active catalytic center. Electrochemical measurements in 0.1 M KOH show that the special atomic arrangement plays an important role in the increased alkaline ORR activity of $Pd_{20}Te_7$ nanosheets, with a relatively high mass activity of 0.30 A mg_{Pd}^{-1} at 0.90 V *versus* the RHE. Furthermore, $Pd_{20}Te_7$ nanosheets display significant stability under chronopotentiometry conditions in a mixture of methanol and KOH for more than 50 000 s with negligible activity decay. DFT calculations demonstrate that the high-performance of the $Pd_{20}Te_7$ nanosheets can be attributed to a break in the linear relationship between OOH* and OH* adsorption, which leaves enough room for increased ORR activity but inhibits the methanol oxidation reaction (Fig. 4g and h).

Ethanol oxidation reaction

Recently, controlling the crystal structures of NCs has been used to prepare nanomaterials with novel phases for improving their EOR performance. For example, $L1_2$-Pt_3Zr and hcp-Pt_3Zr were prepared by controlling the temperature of heat treatment to investigate the effect of the crystal structure of Pt_3Zr on its EOR performance.[57] Specifically, by annealing the Pt_3Zr alloy at 900 °C or 1000 °C $L1_2$-Pt_3Zr (space group: $Fm\bar{3}m$) or hcp-Pt_3Zr (space group: $P6_3/mmc$) can be obtained, respectively (Fig. 5a–c). The lattice parameters of hcp-Pt_3Zr are determined to be $a = b = 5.741$ Å, $c = 9.381$ Å, $\alpha = \beta = 90^\circ$ and $\gamma = 120^\circ$. On the other hand, the unit cell parameters of $L1_2$-Pt_3Zr are $a = b = c = 4.056$ Å and $\alpha = \beta = \gamma = 90^\circ$. Notably, the crystal structure analysis indicates that the average interatomic distance between Zr and the nearest neighboring Pt atoms is 0.2815 nm in hcp-Pt_3Zr, which is shorter than that of 0.2841 nm in $L1_2$-Pt_3Zr. The shorter Pt–Zr bond in hcp-Pt_3Zr indicates that the Pt–Zr bonds are stronger in hcp-Pt_3Zr than in $L1_2$-Pt_3Zr. Interestingly, the electrochemical tests show that hcp-Pt_3Zr exhibits a higher EOR activity (peak current: 0.886 mA cm^{-2}) than Pt/C (peak current: 0.455 mA cm^{-2}) and $L1_2$-Pt_3Zr (peak current: 0.661 mA cm^{-2}). Theoretical calculations indicate that hcp-Pt_3Zr has a higher surface energy than $L1_2$-Pt_3Zr, which facilitates the adsorption/decomposition of ethanol/formic acid molecules on the surface.

Unconventional Pd-based intermetallic compounds also exhibit great development potential for the alkaline EOR due to their promising activity and stability under alkaline conditions. For instance, Huang *et al.* synthesized rhombohedral Pd_8Sb_3 nanosheets through chemical reduction of palladium(II) acetylacetonate ($Pd(acac)_2$) and antimony trichloride ($SbCl_3$) in the presence of polyvinyl pyrrolidone (PVP), benzyl alcohol (BP) and ammonia bromide (NH_4Br).[62] The lattice parameters of Pd_8Sb_3 are determined to be $a = b = c = 15.275$ Å and $\alpha = \beta = \gamma = 29.265^\circ$. Electrochemical tests show that Pd_8Sb_3/C has an MA of 4.5 A mg_{Pd}^{-1} and SA of 29.3 mA cm^{-2} at 0.9 V in 0.5 M NaOH and 0.5 M ethanol solution, which are 7 and 9.8 times higher than those of Pd/C and benchmark Pt/C, respectively. *In situ* electrochemical attenuated total reflectance surface enhanced infrared absorption spectroscopy (ATR-SEIRAS)

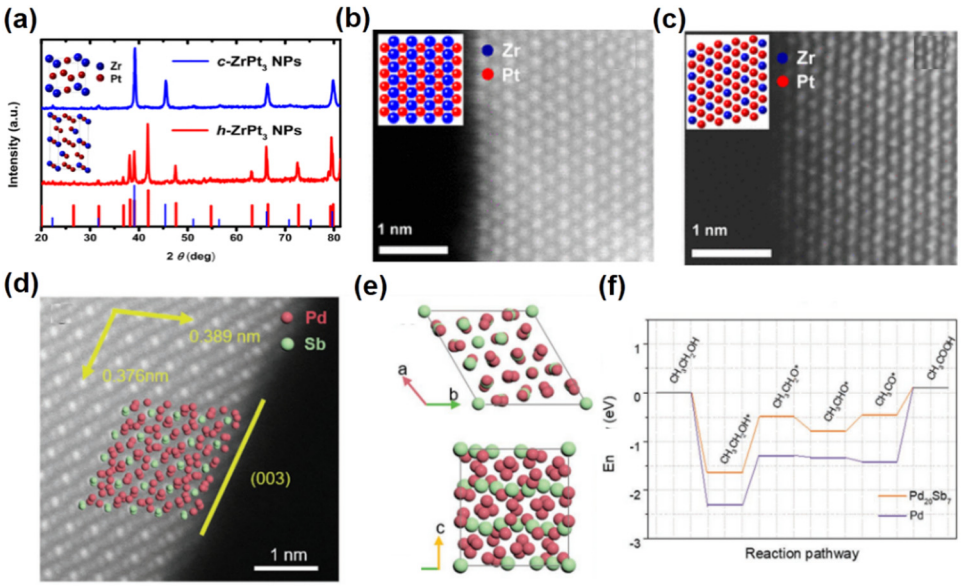

Fig. 5 (a) XRD pattern of the Pt_3Zr nanoparticles annealed at 900 °C and 1000 °C. (b) Aberration-corrected HAADF-STEM image of $L1_2$-Pt_3Zr. (c) Aberration-corrected HAADF-STEM image of hcp-Pt_3Zr. Reproduced with permission from Ref. 57. Copyright 2014, American Chemical Society. (d) Aberration-corrected HAADF-STEM images of $Pd_{20}Sb_7$ rhombohedra. (e) Crystal structure model of $Pd_{20}Sb_7$. (f) Calculated free energy profiles for the EOR based on $Pd_{20}Sb_7$ and Pd. (d)–(f) Reproduced with permission from Ref. 63. Copyright 2022, John Wiley and Sons.

measurements and DFT calculations reveal that Pd_8Sb_3/C can effectively optimize the C_2 pathway of the EOR, which can reduce the energy barrier of ethanol dehydrogenation. Furthermore, the unconventional $Pd_{20}Sb_7$ rhombohedra with the rhombohedral phase were prepared by increasing the amount of reducing agent (Fig. 5d and e).[63] The lattice parameters of $Pd_{20}Sb_7$ are determined to be $a = b = c = 7.834$ Å and $\alpha = \beta = \gamma = 99.148^\circ$. Benefiting from the high proportion of the unique exposed (003) surface, $Pd_{20}Sb_7$ rhombohedra exhibit a much enhanced EOR performance compared to commercial Pd/C. The MA of $Pd_{20}Sb_7$/C was 3.48 A mg_{Pd}^{-1}, which was 8.9 times higher than that of commercial Pd/C. DFT calculations reveal that the unique exposed facets of $Pd_{20}Sb_7$ rhombohedra can not only reduce the excessive adsorption of CH_3CO^* to CH_3COOH on Pd sites for promoting the EOR process, but also weaken CO binding and CO poisoning (Fig. 5f). This work highlights the significant role of unconventional intermetallic phases and morphology design in electrocatalysis.

4. Summary and outlook

The regulation of the properties of catalysts has traditionally focused on controlling their size, morphology and crystalline surface. However, these modifications only involve the arrangement of atoms on the surface, which are susceptible to collapse under acidic and high voltage conditions. Recent works have demonstrated that altering the arrangement of all atoms inside the nanocrystal by engineering the crystal structure of a catalyst can also dramatically enhance its catalytic performance. Here, we have briefly introduced appropriate synthetic methodologies to manufacture unconventional intermetallic noble metal-based NCs for energy conversion. Several representative examples are presented (Table 1). To stimulate more fascinating efforts towards the development of unconventional intermetallic catalysts, much exploration needs to be further pursued.

Clarifying the relationship between the crystal structure and the improved performance

Although significant progress has been made on the catalytic study of unconventional intermetallic NCs, the relationship between crystal phases and electrocatalytic performance is still unclear. Specifically, limited by the complex thermodynamic and kinetic parameters of the synthesis process, variations in the particle size and morphology usually occur during the synthesis of catalysts with different phases, leading to difficulties in independently investigating the role of their crystal structures in improving their performance. In order to deeply analyze and compare the activity differences of different crystal phases, it is critical to maintain a similar morphology and particle size of NCs through precise control of synthetic parameters. In addition, advanced characterization techniques (*e.g.*, X-ray absorption spectroscopy and Raman spectroscopy) and theoretical analysis (*e.g.*, DFT calculations) would provide useful knowledge about the bond lengths, coordination numbers, electronic structures, surface adsorption properties and catalytic reaction pathways of catalysts with various phases. The correlated investigation of crystal phase-activity relationship will contribute to the design of novel electrocatalysts with outstanding performance.

Investigating the formation process and evolution mechanism of unconventional intermetallic compounds

The process of phase transition and the evolution mechanism of solid-state materials are complicated. Clarifying the mechanism of phase formation and transformation by *in situ* characterization techniques can provide fundamental directions for the design of the crystal phase of catalysts and the further exploitation of controlled methods. For example, *in situ* high-resolution transmission electron microscopy and X-ray diffraction make it possible to recognize the phase transition mechanisms, phase transition rates and intermediate states. In addition, the combination of theoretical calculations would also be beneficial for

Table 1 Summary of representative intermetallic nanocatalysts with unconventional phases for energy conversion

Material	Crystal system (space group)	Application (electrolyte)	Performance	Ref.
IrMo/CNT	Orthorhombic (*Pmma*)	HER (1 M KOH)	Overpotential of 17 mV at 10 mA cm^{-2}	46
IrGa/N-rGO	Cubic ($Pm\bar{3}m$)	HER (1 M KOH)	Overpotential of 22 mV at 10 mA cm^{-2}	48
PdCu	Cubic ($Pm\bar{3}m$)	HER (0.5 M H_2SO_4)	Overpotential of 19.7 mV at 10 mA cm^{-2}	50
RuGa	Cubic ($Pm\bar{3}m$)	HER (1 M KOH)	Overpotential of 156 mV at 1000 mA cm^{-2}	49
PtSi	Orthorhombic (*Pnma*)	HER (0.5 M H_2SO_4)	Overpotential of 22 mV at 10 mA cm^{-2}	51
Ru_3Sn_7	Cubic ($Im\bar{3}m$)	HER (0.5 M H_2SO_4)	Overpotential of 28 mV at 10 mA cm^{-2}	58
PtPb nanoplates	Hexagonal ($P6_3/mmc$)	ORR (0.1 M $HClO_4$)	Mass activity of 4.3 A mg_{Pt}^{-1} at 0.9 V	52
Pt_5Ce	Hexagonal ($P6/mmm$)	ORR (0.1 M $HClO_4$)	Mass activity of 0.7 A mg_{Pt}^{-1} at 0.9 V	54
Pt_5La	Hexagonal ($P6/mmm$)	ORR (0.1 M $HClO_4$)	Mass activity of 0.657 A mg_{Pt}^{-1} at 0.9 V	59
PtCu	Trigonal ($R\bar{3}m$)	ORR (0.1 M $HClO_4$)	Mass activity of 2.5 A mg_{Pt}^{-1} at 0.9 V	60
$Pd_{31}Bi_{12}$	Hexagonal ($R3$)	ORR (0.1 M KOH)	Specific activity of 9.20 mA cm_{Pd}^{-2} at 0.9 V	61
Pd_5Bi_2	Monoclinic ($C2/m$)	ORR (0.1 M KOH)	Mass activity of 2.05 A mg_{Pd}^{-1} at 0.9 V	55
$Pd_{17}Se_{15}$	Cubic ($Pm\bar{3}m$)	ORR (0.1 M KOH)	Mass activity of 0.46 A mg_{Pd}^{-1} at 0.90 V	29
$Pd_{20}Te_7$	Trigonal ($R\bar{3}$)	ORR (0.1 M KOH)	Mass activity of 0.30 A mg_{Pd}^{-1} at 0.90 V	56
Pt_3Zr	Hexagonal ($P6_3/mmc$)	EOR (1 M ethanol/0.5 M H_2SO_4)	Peak current of 0.886 mA cm^{-2}	57
Pd_8Sb_3	Hexagonal ($R3c$)	EOR (0.5 M ethanol/0.5 M NaOH)	Mass activity of 4.5 A mg_{Pd}^{-1}	62
$Pd_{20}Sb_7$	Trigonal ($R\bar{3}$)	EOR (0.5 M ethanol/0.5 M NaOH)	Mass activity of 3.48 A mg_{Pd}^{-1}	63
PtBi	Hexagonal ($P6_3/mmc$)	MOR (0.5 M CH_3OH/1 M KOH)	Mass activity of 6.79 A mg_{Pt}^{-1}	64
PtSnBi	Hexagonal ($P6_3/mmc$)	MOR (0.5 M CH_3OH/1 M KOH)	Mass activity of 7.02 A mg_{Pt}^{-1}	65

determining the formation energies of different phases, the energy barriers of different transition paths, the movement paths of atoms, *etc*.

Exploring applications in extended electrocatalytic reactions and the scale-up preparation of unconventional intermetallic compounds

Despite the fact that the unconventional intermetallic compounds have been investigated in electrocatalytic water splitting (*e.g.* the HER) and fuel cells (*e.g.* the ORR and EOR), their catalytic properties in other chemical reactions have been less explored. Therefore, their applications in clean energy conversion and catalysis need to be further explored. Furthermore, in order to obtain the desired structure, size and morphology, researchers usually adopt small batch and meticulous methods to produce unconventional intermetallic compounds in the laboratory. However, in view of the demand for industrial applications, the large-scale preparation of unconventional intermetallic compounds is worth further exploration.

Conflicts of interest

The authors declare no conflicts of interest.

Acknowledgements

This work was financially supported by the National Natural Science Foundation of China (22122202, 21972051, and 22072051).

References

1 M. Shao, Q. Chang, J. P. Dodelet and R. Chenitz, *Chem. Rev.*, 2016, **116**, 3594–3657.
2 S. Anantharaj, S. R. Ede, K. Sakthikumar, K. Karthick, S. Mishra and S. Kundu, *ACS Catal.*, 2016, **6**, 8069–8097.
3 J. Mei, T. Liao, L. Kou and Z. Sun, *Adv. Mater.*, 2017, **29**, 1700176.
4 J. Liang, F. Ma, S. Hwang, X. Wang, J. Sokolowski, Q. Li, G. Wu and D. Su, *Joule*, 2019, **3**, 956–991.
5 D. Banham and S. Ye, *ACS Energy Lett.*, 2017, **2**, 629–638.
6 A. Kongkanand and M. F. Mathias, *J. Phys. Chem. Lett.*, 2016, **7**, 1127–1137.
7 J. Lai, S. Chen, X. Liu, X. Yan, Z. Qin, L. Xie, Z. Lin, Z. Cai, Y. Zhao, H.-L. Wang, Y. Huang and Q. Li, *ACS Catal.*, 2023, **13**, 11996–12006.
8 Y. Z. Hui-Fang Yuan, Xing-Wu Zhai, Li-Bing Hu, Gui-Xian Ge, Gang Wang, Feng Yu and Bin Dai, *J. Electrochem.*, 2021, **27**, 671–680.
9 T. Wang, H. Xie, M. Chen, A. D'Aloia, J. Cho, G. Wu and Q. Li, *Nano Energy*, 2017, **42**, 69–89.
10 H. Shi, T. Wang, J. Liu, W. Chen, S. Li, J. Liang, S. Liu, X. Liu, Z. Cai, C. Wang, D. Su, Y. Huang, L. Elbaz and Q. Li, *Nat. Commun.*, 2023, **14**, 3934.
11 J. Mei, Y. Deng, X. Cheng, X. Wang and Q. Wu, *Chin. Chem. Lett.*, 2024, **35**, 108900.
12 D. S. He, D. He, J. Wang, Y. Lin, P. Yin, X. Hong, Y. Wu and Y. Li, *J. Am. Chem. Soc.*, 2016, **138**, 1494–1497.
13 Z. Miao, X. Wang, M. C. Tsai, Q. Jin, J. Liang, F. Ma, T. Wang, S. Zheng, B. J. Hwang, Y. Huang, S. Guo and Q. Li, *Adv. Energy Mater.*, 2018, **8**, 1801226.
14 Z. Miao, X. Wang, Z. Zhao, W. Zuo, S. Chen, Z. Li, Y. He, J. Liang, F. Ma, H.-L. Wang, G. Lu, Y. Huang, G. Wu and Q. Li, *Adv. Mater.*, 2021, **33**, 2006613.
15 D. A. Kuznetsov, B. Han, Y. Yu, R. R. Rao, J. Hwang, Y. Román-Leshkov and Y. Shao-Horn, *Joule*, 2018, **2**, 225–244.
16 T. Wang, G. Nam, Y. Jin, X. Wang, P. Ren, M. G. Kim, J. Liang, X. Wen, H. Jang, J. Han, Y. Huang, Q. Li and J. Cho, *Adv. Mater.*, 2018, **30**, e1800757.
17 J. Mahmood, F. Li, S. M. Jung, M. S. Okyay, I. Ahmad, S. J. Kim, N. Park, H. Y. Jeong and J. B. Baek, *Nat. Nanotechnol.*, 2017, **12**, 441–446.
18 H. Wang and H. D. Abruna, *J. Am. Chem. Soc.*, 2017, **139**, 6807–6810.
19 J. Sun, X. Lao, M. Yang, A. Fu, J. Chen, M. Pang, F. Gao and P. Guo, *Langmuir*, 2021, **37**, 14930–14940.
20 Y. Ge, X. Wang, B. Chen, Z. Huang, Z. Shi, B. Huang, J. Liu, G. Wang, Y. Chen, L. Li, S. Lu, Q. Luo, Q. Yun and H. Zhang, *Adv. Mater.*, 2022, **34**, e2107399.
21 M. Zhou, J. Liu, C. Ling, Y. Ge, B. Chen, C. Tan, Z. Fan, J. Huang, J. Chen, Z. Liu, Z. Huang, J. Ge, H. Cheng, Y. Chen, L. Dai, P. Yin, X. Zhang, Q. Yun, J. Wang and H. Zhang, *Adv. Mater.*, 2022, **34**, e2106115.
22 J. Zhu, Y. Yang, L. Chen, W. Xiao, H. Liu, H. D. Abruña and D. Wang, *Chem. Mater.*, 2018, **30**, 5987–5995.
23 J. Wang, J. Zhang, G. Liu, C. Ling, B. Chen, J. Huang, X. Liu, B. Li, A.-L. Wang, Z. Hu, M. Zhou, Y. Chen, H. Cheng, J. Liu, Z. Fan, N. Yang, C. Tan, L. Gu, J. Wang and H. Zhang, *Nano Res.*, 2020, **13**, 1970–1975.
24 H. Huang, K. Li, Z. Chen, L. Luo, Y. Gu, D. Zhang, C. Ma, R. Si, J. Yang, Z. Peng and J. Zeng, *J. Am. Chem. Soc.*, 2017, **139**, 8152–8159.
25 L. Gao, X. Li, Z. Yao, H. Bai, Y. Lu, C. Ma, S. Lu, Z. Peng, J. Yang, A. Pan and H. Huang, *J. Am. Chem. Soc.*, 2019, **141**, 18083–18090.
26 J. Li, Z. Xi, Y.-T. Pan, J. S. Spendelow, P. N. Duchesne, D. Su, Q. Li, C. Yu, Z. Yin, B. Shen, Y. S. Kim, P. Zhang and S. Sun, *J. Am. Chem. Soc.*, 2018, **140**, 2926–2932.
27 D. Wang, H. L. Xin, R. Hovden, H. Wang, Y. Yu, D. A. Muller, F. J. DiSalvo and H. D. Abruna, *Nat. Mater.*, 2013, **12**, 81–87.
28 J. Liang, N. Li, Z. Zhao, L. Ma, X. Wang, S. Li, X. Liu, T. Wang, Y. Du, G. Lu, J. Han, Y. Huang, D. Su and Q. Li, *Angew. Chem., Int. Ed.*, 2019, **58**, 15471–15477.
29 Z. Yu, S. Xu, Y. Feng, C. Yang, Q. Yao, Q. Shao, Y. F. Li and X. Huang, *Nano Lett.*, 2021, **21**, 3805–3812.
30 Y. Nanba and M. Koyama, *Comput. Mater. Sci.*, 2022, **203**, 111132.
31 A. J. Medford, A. Vojvodic, J. S. Hummelshøj, J. Voss, F. Abild-Pedersen, F. Studt, T. Bligaard, A. Nilsson and J. K. Nørskov, *J. Catal.*, 2015, **328**, 36–42.

32 Y. Yan, J. S. Du, K. D. Gilroy, D. Yang, Y. Xia and H. Zhang, *Adv. Mater.*, 2017, **29**, 1605997.
33 X. Fu, H. Li, A. Xu, F. Xia, L. Zhang, J. Zhang, D. Ma, J. Wu, Q. Yue, X. Yang and Y. Kang, *Nano Lett.*, 2023, **23**, 5467–5474.
34 L. Gao, F. Bao, X. Tan, M. Li, Z. Shen, X. Chen, Z. Tang, W. Lai, Y. Lu, P. Huang, C. Ma, S. C. Smith, Z. Ye, Z. Hu and H. Huang, *Energy Environ. Sci.*, 2023, **16**, 285–294.
35 P. Li, Y. Jiang, Y. Hu, Y. Men, Y. Liu, W. Cai and S. Chen, *Nat. Catal.*, 2022, **5**, 900–911.
36 C. Cai, K. Liu, L. Zhang, F. Li, Y. Tan, P. Li, Y. Wang, M. Wang, Z. Feng, D. Motta Meira, W. Qu, A. Stefancu, W. Li, H. Li, J. Fu, H. Wang, D. Zhang, E. Cortés and M. Liu, *Angew. Chem., Int. Ed.*, 2023, **62**, e202300873.
37 Y. Ji, Z. Chen, R. Wei, C. Yang, Y. Wang, J. Xu, H. Zhang, A. Guan, J. Chen, T.-K. Sham, J. Luo, Y. Yang, X. Xu and G. Zheng, *Nat. Catal.*, 2022, **5**, 251–258.
38 J. Liang, Z. Zhao, N. Li, X. Wang, S. Li, X. Liu, T. Wang, G. Lu, D. Wang, B. J. Hwang, Y. Huang, D. Su and Q. Li, *Adv. Energy Mater.*, 2020, **10**, 2000179.
39 X. Liu, Z. Zhao, J. Liang, S. Li, G. Lu, C. Priest, T. Wang, J. Han, G. Wu, X. Wang, Y. Huang and Q. Li, *Angew. Chem., Int. Ed.*, 2023, **62**, e202302134.
40 Y. Hu, J. O. Jensen, L. N. Cleemann, B. A. Brandes and Q. Li, *J. Am. Chem. Soc.*, 2020, **142**, 953–961.
41 D. Y. Chung, J. M. Yoo and Y.-E. Sung, *Adv. Mater.*, 2018, **30**, 1704123.
42 P. P. Lopes, D. Strmcnik, D. Tripkovic, J. G. Connell, V. Stamenkovic and N. M. Markovic, *ACS Catal.*, 2016, **6**, 2536–2544.
43 M. Wang, L. Wang, H. Li, W. Du, M. U. Khan, S. Zhao, C. Ma, Z. Li and J. Zeng, *J. Am. Chem. Soc.*, 2015, **137**, 14027–14030.
44 M. Zhou, C. Li and J. Fang, *Chem. Rev.*, 2021, **121**, 736–795.
45 H. Li, H. Huang, Y. Chen, F. Lai, H. Fu, L. Zhang, N. Zhang, S. Bai and T. Liu, *Adv. Mater.*, 2023, **35**, 2209242.
46 J. Zhang, L. Zhang, J. Liu, C. Zhong, Y. Tu, P. Li, L. Du, S. Chen and Z. Cui, *Nat. Commun.*, 2022, **13**, 5497.
47 H. Itahara, Y. Takatani, N. Takahashi, S. Kosaka, A. Nagoya, M. Inaba, Y. Kamitaka and Y. Morimoto, *Chem. Mater.*, 2021, **34**, 422–429.
48 H. Zhang, P. Shi, X. Ma, C. Ma, S. Han, C. He, H. Wu, L. Zhu, B. Zhang, Y. Lu, W. Cao, H. Yin, X. Meng, J. Xia, J. Zhang, A. L. Wang and Q. Lu, *Adv. Energy Mater.*, 2022, **13**, 2202703.
49 H. Zhang, C. Cheng, J. Zhou, C. Ma, P. Shi, H. Wu, P. Yin, W. Cao, J. Xia, L. Zhu, A.-L. Wang and Q. Lu, *J. Mater. Chem. A*, 2023, **11**, 10328–10336.
50 M. M. Flores Espinosa, T. Cheng, M. Xu, L. Abatemarco, C. Choi, X. Pan, W. A. Goddard, Z. Zhao and Y. Huang, *ACS Energy Lett.*, 2020, **5**, 3672–3680.
51 Z. Pu, T. Liu, G. Zhang, Z. Chen, D. S. Li, N. Chen, W. Chen, Z. Chen and S. Sun, *Adv. Energy Mater.*, 2022, 12.
52 L. Bu, N. Zhang, S. Guo, X. Zhang, J. Li, J. Yao, T. Wu, G. Lu, J.-Y. Ma, D. Su and X. Huang, *Science*, 2016, **354**, 1410–1414.
53 T. Gunji, S. Tanaka, T. Inagawa, K. Otsuka and F. Matsumoto, *ACS Appl. Nano Mater.*, 2022, **5**, 4958–4965.
54 S. Xu, S. Zhao, W. Zeng, S. Li, M. Zuo, Y. Lin, S. Chu, P. Chen, J. Liu and H. Liang, *Chem. Mater.*, 2022, **34**, 10789–10797.
55 M. Zhou, J. Guo, B. Zhao, C. Li, L. Zhang and J. Fang, *J. Am. Chem. Soc.*, 2021, **143**, 15891–15897.
56 Y. Zhang, B. Huang, G. Luo, T. Sun, Y. Feng, Y. Wang, Y. Ma, Q. Shao, Y. Li, Z. Zhou and X. Huang, *Sci. Adv.*, 2020, **6**, eaba9731.
57 G. V. Ramesh, R. Kodiyath, T. Tanabe, M. Manikandan, T. Fujita, N. Umezawa, S. Ueda, S. Ishihara, K. Ariga and H. Abe, *ACS Appl. Mater. Interfaces*, 2014, **6**, 16124–16130.
58 Z. Wang, Z. Lin, Y. Wang, S. Shen, Q. Zhang, J. Wang and W. Zhong, *Adv. Mater.*, 2023, **35**, 2302007.
59 T. Gunji, S. Tanaka, T. Inagawa, K. Otsuka and F. Matsumoto, *ACS Appl. Nano Mater.*, 2022, **5**, 4958–4965.
60 H. Y. Kim, T. Kwon, Y. Ha, M. Jun, H. Baik, H. Y. Jeong, H. Kim, K. Lee and S. H. Joo, *Nano Lett.*, 2020, **20**, 7413–7421.
61 Y. Wang, D. Sun, T. Chowdhury, J. S. Wagner, T. J. Kempa and A. S. Hall, *J. Am. Chem. Soc.*, 2019, **141**, 2342–2347.
62 Y. Zhang, X. Liu, T. Liu, X. Ma, Y. Feng, B. Xu, W. Cai, Y. Li, D. Su, Q. Shao and X. Huang, *Adv. Mater.*, 2022, **34**, e2202333.
63 B. Xu, T. Liu, X. Liang, W. Dou, H. Geng, Z. Yu, Y. Li, Y. Zhang, Q. Shao, J. Fan and X. Huang, *Adv. Mater.*, 2022, **34**, e2206528.
64 J. Zhang, M. Yuan, T. Zhao, W. Wang, H. Huang, K. Cui, Z. Liu, S. Li, Z. Li and G. Zhang, *J. Mater. Chem. A*, 2021, **9**, 20676–20684.
65 J. Zhang, T. Zhao, M. Yuan, Z. Li, W. Wang, Y. Bai, Z. Liu, S. Li and G. Zhang, *J. Colloid Interface Sci.*, 2021, **602**, 504–512.